Experimental evidence of quadrupolar whispering-gallery modes in phononic crystal based waveguides

Jinfeng Zhao, Weitao Yuan, Olga Boyko, Bernard Bonello, Xiaoqing Zhang, Yongdong P Pan, Zheng Zhong

HAL Id: hal-02297773
https://hal.sorbonne-universite.fr/hal-02297773

Submitted on 26 Sep 2019

Experimental evidence of quadrupolar whispering-gallery modes in phononic crystal based waveguides

Jinfeng Zhao (iD), Weitao Yuan, Olga Boyko, Bernard Bonello (iD), Xiaoqing Zhang (iD), Yongdong Pan (iD), and Zheng Zhong

ARTICLES YOU MAY BE INTERESTED IN

Experimental evidence of quadrupolar whispering-gallery modes in phononic crystal based waveguides

View Online   Export Citation   CrossMark

Jinfeng Zhao,[1,a),b)] (iD) Weitao Yuan,[1,b)] Olga Boyko,[2] Bernard Bonello,[2] (iD) Xiaoqing Zhang,[3] (iD) Yongdong Pan,[1] (iD) and Zheng Zhong[1,4,a)]

AFFILIATIONS

[1] School of Aerospace Engineering and Applied Mechanics, Tongji University, 100 Zhangwu Road, 200092 Shanghai, China
[2] Sorbonne Université, UPMC Université Paris 06, INSP UMR CNRS 7588, 4 Place Jussieu, 75005 Paris, France
[3] School of Physics Science and Engineering, Tongji University, 1239 Siping Road, 200092, Shanghai, China
[4] School of Science, Harbin Institute of Technology, Shenzhen 518055, China

[a)]**Corresponding authors:** jinfeng.zhao@tongji.edu.cn, zhongzheng@hit.edu.cn
[b)]**Contributions:** J. Zhao and W. Yuan contributed equally to this work.

ABSTRACT

Understanding the performance of resonators introduced in elastic and/or acoustic circuits is important for conceiving complex and efficient guiding structures. In this work, we reported upon the experimental characterization of hollow pillars in different waveguides with 90° corners by measuring the displacement on top of hollow pillars. The air-coupled method, laser ultrasonic technique and the newly developed method based on polypropylene (PP) piezoelectret film have been adopted during this process. In such way, we experimentally show the quadrupolar resonance of hollow pillars that corresponds well to the whispering-gallery modes in numerical results in several types of waveguides for guiding Lamb wave.

I. INTRODUCTION

It is acknowledged that phonon works as a kind of quasiparticle after electron and photon.[1] Inspired by the significant progress of controlling of electrons in semiconductor or photons in photonic crystals, the controlling of mechanical waves has attracted growing interest based on many structures. Among them, phononic crystals (PCs) are the artificially periodic structures used to manipulate the propagation of acoustic/elastic waves, which can provide much functionality beyond traditional materials,[2–5] such as acoustic cloaking,[2,3] superlensing[4] and subwavelength imaging.[5] As a result, PCs based structures have broad prospective applications in many fields such as sensors[6] and acoustics lens.[7]

Recently, with the development of on-chip technology and the demand for integrated devices, PC based waveguides have obtained much attention for their importance to the acoustic circuits. Generally, these waveguides are constructed by removing scatterers along a straight line or other designed routes from perfect PCs. However, this kind of waveguide can have a broad band over a large part of the stop band, or encounter transmission dips because of the occurrence of sharp corners in route lines.[8–10] Inspired by the whispering gallery modes (WGMs) and their applications in optical fields,[11–13] there have been growing works on implementing WGMs into the acoustic circuits. Back in 2003 and 2004, a group of researchers studied numerically the propagation and guiding of acoustic waves in two-dimensional PCs composed of hollow scatterers in fluid.[14,15] Later, they noticed that utilizing hollow pillars can give rise to waveguides for selected frequency, which shall be attributed to the occurrence of WGMs in hollow pillars.[16]

Quite recently, Yuan et al reported the experimental evidences of compact waveguide[17] and the rainbow guiding phenomenon[18]

for the lowest-order antisymmetric Lamb (A_0) wave based on the quadrupolar WGMs in hollow pillars in different waveguides. Wang *et al* also constructed waveguides by engraving hollow pillars into the triangle-latticed perfect PCs, and demonstrated the energy localization at the foot of hollow pillars.[19] The acoustic transmission through the waveguides has been characterized in these works. Indeed, the high-order multi-polar resonances in hollow pillars, e.g. quadrupolar WGMs, bring additional degree for controlling phonons since they can carry even more information. Such effect has been observed when using WGMs to control the propagation of acoustic/elastic waves and the energy distribution after the waveguides.[17] Therefore, the WGMs are potential for conceiving complex and efficient integrated acoustic circuits. To this end, the fine regulation of vibration in resonators is a prerequisite in order to make full utilization of WGMs. The direct experimental characterization of displacement field on top of hollow pillars can be helpful for understanding the performance and mechanism of these resonators, which is however still lacking in previous works. In some other works, researchers have measured the distribution of displacement on top of solid pillars and studied the coupling between propagative modes in the substrate and the monopolar or dipolar resonance in pillars.[20,21] This confirms possibility of measuring the out-of-plane displacement on top of pillars.

In this work, we built different waveguides for A_0 wave in reconfigurable manners based on the WGMs in hollow pillars. We investigated both numerically and experimentally the displacement field on top of the hollow pillars in these structures, and we show the direct experimental evidence of the quadrupolar WGMs in hollow pillars. This paper is organized as follows. Section II describes the sample details and the dispersion curves of unit cells, while Section III presents the experimental configuration. After that, the presentation and analysis of both the numerical and experimental results are given in Section IV followed by the Conclusions in Section V.

II. SAMPLE DETAILS AND DISPERSION CURVES

We constructed different waveguides by inserting hollow pillars in between arrays of square-latticed solid pillars along three designated paths including the i) straight waveguide (see Fig. 3(a)), ii) Z-shaped waveguide with two 90° corners (see Fig. 6(a)), and iii) π-shaped waveguide with three 90° corners (see Fig. 9(a)). Both the hollow and solid pillars were made of steel and were cemented by the epoxy adhesive to one side of the aluminum plate. For the convenience of analysis, we built a square-latticed unit cell that combined a cap hollow steel pillar, a middle epoxy resin pillar and a bottom aluminum plate. The height, outer diameter and inner diameter of the cap steel pillars are h_p, d_1, d_2, respectively. The middle epoxy resin layer was assumed featuring the same outer and inner diameters as the cap steel pillar with a different height h_g. The lattice constant is a, and the thickness of aluminum substrate is e. We set the geometrical parameters (in mm) $d_1 = 5$, $a = 6$, $e = 1.5$, and $h_g = 0.135$.[17,18,21] Regarding the material properties, we used the Young's modulus 199 GPa, Possion's ratio 0.25, and mass density 7850 kg/m³ for the Q304 steel; 5.1 GPa, 0.38, 1200 kg/m³ for the epoxy resin; 67.7 GPa, 0.35, 2700 kg/m³ for the aluminum.

We then calculated the dispersion of PC plate with either the hollow pillar (hollow PC) or solid pillar (solid PC) by using the finite-element method (FEM). The blue circle lines in Figs. 1(a) and 1(b) show the dispersion curves of the solid PC plate when $h_p = 5$ mm and $d_2 = 0$, magnifying a complete stop band in between 163 kHz and 243 kHz. The dispersion curves of the hollow PC are given by the dotted lines in Fig. 1(a) when $h_p = 2.5$ mm and $d_2 = 2.56$ mm or in Fig. 1(b) when $h_p = 2.5$ mm and $d_2 = 2.7$ mm. In contrast to the case of solid PC plate, two new branches that belong to the hollow PC plate appear in between 188 and 201 kHz in Fig. 1(a), or in a lower frequency range between 177 and 189 kHz in Fig. 1(b). Figures 1(c) and 1(d) show the normalized total displacement u_t and the deformation at point X of Brillouin zone (BZ) on the green (187.9 kHz) or red line (186.6 kHz) in Fig. 1(b), respectively. Obviously, the hollow pillar in Fig. 1(c) shows the quadrupolar pattern and two polarized axes in parallel to x and y axes, as indicated by the black arrows. We call this mode WGM 1 hereafter. The hollow pillar in Fig. 1(d) has two polarized axes featuring angle ±45° to x or y axis, which we called as WGM 2. The same model shapes can be found at X of BZ in Fig. 1(a) when $d_2 = 2.56$ mm at the green or red line.
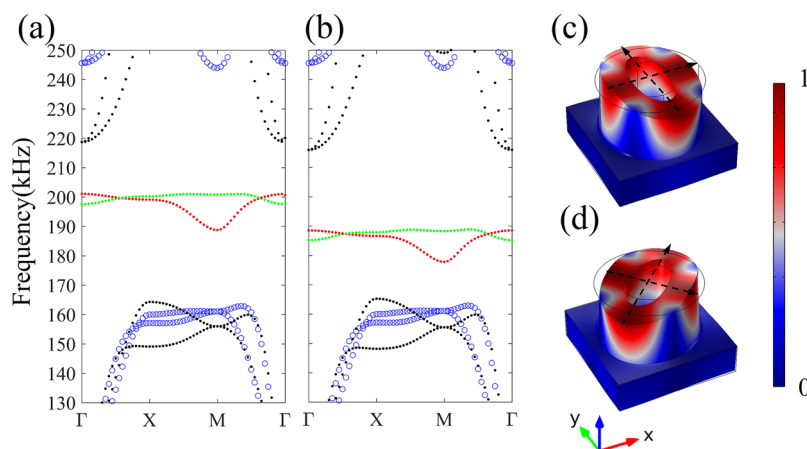
FIG. 1. Band structures of the hollow PC plate (black dotted lines) wherein the (in mm) $a = 6$, $e = 1.5$, $h_g = 0.135$, $h_p = 2.5$, $d_1 = 5$, (a) $d_2 = 2.56$ or (b) $d_2 = 2.7$, and the counterparts of the solid PC plate ($d_2 = 0$) when $h_p = 5$ (blue circle lines). In both figures, the green and red lines represent the branches of WGM 1 and WGM 2, respectively, for which the normalized distribution of total displacement u_t and the modal shapes are given in (c) and (d) in order, retrieved at X of BZ in Fig. 1(b).
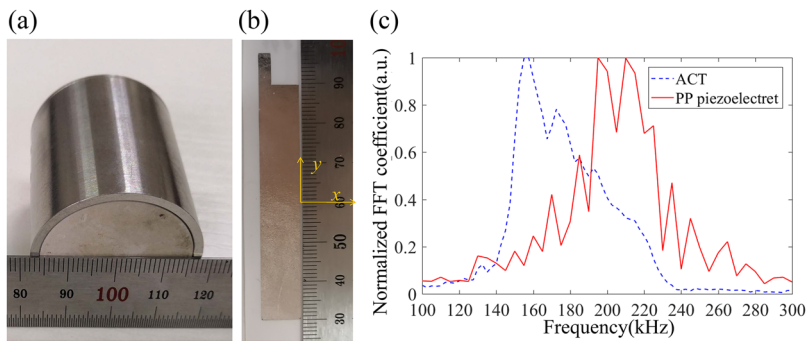
FIG. 2. Photograph of (a) the air-coupled transducer or (b) PP piezoelectret film. (c) Normalized amplitude of Fourier transformation (FFT) coefficient of measured u_z when using the ACT (blue dashed line) or PP piezoelectret film (red solid line) with exciting frequency f = 200 kHz.

III. EXPERIMENTAL SETUPS

In experimental setup, we used two configurations to excite the zero-order flexural Lamb (A_0) wave in front of the waveguides according to the frequency requirement. The first was based on the air-coupled method.[22] In this case, an unfocused air-coupled transducer (ACT) (see Fig. 2(a)) was used as the emitter to issue ultrasonic pulses to the aluminum plate in front of the waveguide. By carefully regulating the incident angle of ultrasonic pulses versus the aluminum plate,[22] A_0 wave was generated on the substrate plate with the transverse amplitude following the Gaussian profile. In the second case, we adopted a polypropylene (PP) piezoelectret film,[23,24] as shown in Fig. 2(b), as the emitter that occupied the area (electrode size) 60 mm × 10 mm. This 70 μm thick PP piezoelectret film features a basic resonant frequency about 400 kHz when two sides are free, or about 200 kHz when one side of the PP piezoelectret film is clamped to the substrate, e.g. aluminum plate here, while the other one is free.[23,24] The PP piezoelectret film shall set the aluminum plate into vibration to generate A_0 wave, upon the excitation of the electric signals, just in a way similar to the classic piezoelectric disk. It is noteworthy that the electro-acoustic devices based on PP piezoelectret film have the advantages such as low price, light weight, simple structure, high sensitivity and low impedance.

Concerning the measurement, we used a laser ultrasonic technique based on laser Doppler vibrometer (LDV, Polytec vibrometer OFV 2570) to record the out-of-plane displacement u_z at the points on top of pillars or the aluminum plate.[21,22] Notice that the LDV was fixed to a platform that can be moved freely to allow for the precise selection of measuring points both on top of the pillar and the aluminum plate. Figure 2(c) shows the normalized Fourier transformation coefficient of the signal recorded on the 1.5 mm aluminum plate at a distance 10 mm away from the emitter, by the air-coupled method (blue dashed line) or the PP piezoelectret film (red solid line), both under the excitation signal centered at 200 kHz. The blue dashed line features the peak value at about f_0 = 155 kHz, while the red line magnifies the maximum amplitude at around 200 kHz. The two signals together feature a broad range that cover the interested frequencies for the investigation of waveguides based on WGMs.

IV. NUMERICAL SIMULATION AND EXPERIMENTAL RESULTS

Figure 3(a) shows the photograph of the straight waveguide that consists of two hollow pillars in between solid pillars, wherein the inner diameter of hollow pillars is d_2 = 2.7 mm. Note that the hollow pillars are all 2.5 mm high in this work, because of the strong coupling between WGMs in hollow pillars and propagative modes in aluminum plate, whereas the height of solid pillars is 5 mm all the same for the better confinement of wave energy in the designated route paths.[17] We then built the numerical model whereby the geometric parameters of waveguide are in accordance with the experimental sample, and investigated the performance of the hollow pillars upon the incidence of A_0 wave from the left side by FEM. The numerical model was built up in a same way as those in Ref. 17.
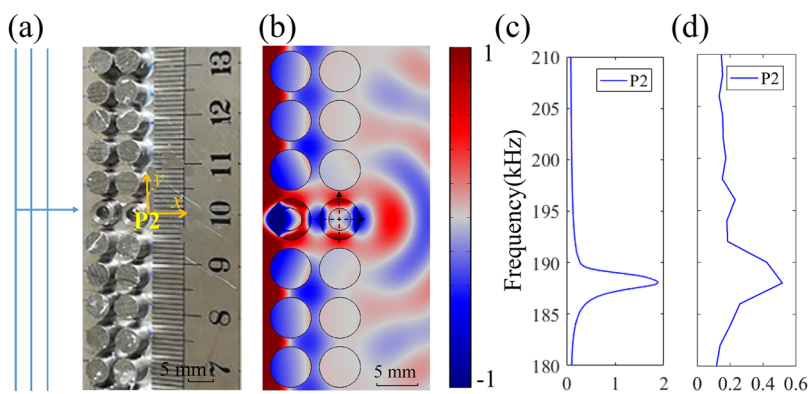
FIG. 3. (a) Top view of straight waveguide with the inner diameter of hollow pillars d_2 = 2.7 mm. (b) Calculated distribution of u_z normalized to the amplitude of incident wave at f = 189 kHz. (c) Calculated and (d) measured average $|u_z|$ on top surface of P2.
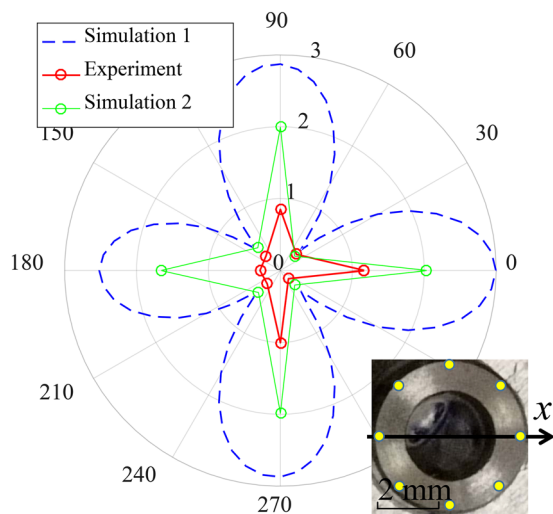
FIG. 4. Polar diagram of computed $|u_z|$ normalized to the amplitude of incident wave at 189 kHz in frequency domain (blue dashed line), in time domain (green solid line) and the measured $|u_z|$ at 188 kHz (red solid line) at points on top of P2 as shown by the yellow symbols in inset.

We labeled the hollow pillar at the outlet as P2 (see Fig. 3(a)). Fig. 3(b) shows the distribution of u_z normalized to the amplitude of incident wave at selected frequency f = 189 kHz, wherein the P2 features two polar axes (black dashed arrows) along the x and y axes as what happens to the WGM 1 in Figs. 1(c) and 1(d). Figures 3(c) and 3(d) show both numerically and experimentally the average amplitude of $|u_z|$ retrieved from eight points (see yellow dots in inset in Fig. 4) on top of P2 versus the amplitude of incident wave. Figure 3(c) shows a peak value at 189 kHz that corresponds well to frequency of WGMs, whereas Fig. 3(d) presents the peak at 188 kHz in good agreement with Fig. 3(c).

We then chose eight points on top of P2 at almost the outer brim with angle 0°, 45°, 90°, 135°, 180°, 225°, 270°, and 315° to the direction of x axis in order, as shown by yellow dots in the inset of Fig. 4. Blue dashed line (labeled as Simulation 1) in Fig. 4 shows

the calculated polar diagram of normalized $|u_z|$ versus the amplitude of incident wave when f = 189 kHz in frequency domain and magnifies four maximum poles at $\theta = 0°$, 90°, 180°, and 270°, which indicates the occurrence of the quadrupolar WGM 1. By adopting the air-coupled method and laser ultrasonic technique, we measured the normalized $|u_z|$ at these points as shown by the red solid line (labeled as Experiment) in Fig. 4 when f = 188 kHz. This experimental profile of $|u_z|$ shows almost the same shape as the numerical counterpart, i.e. three obvious poles at $\theta = 0°$, 90°, and 270°, and another pole at $\theta = 180°$ for the large amplitude in comparison to the adjacent nodes at 135° and 215°. Note that the experimental result in this polar diagram for the peaks at 0°, 90° and 270° are only approximately a third of the amplitude of Simulation 1, also that the experimental amplitude at 180° is much smaller than those at 0°, 90°, 270°. To get a better understanding of the experimental result, we calculated the u_z in time domain and show the result as green solid line (labeled as Simulation 2) in Fig. 4. It is clear that the amplitudes at 0°, 90°, 180° and 270° of Simulation 2 are approximately 2/3 times of those of Simulation 1. The experimental results are about 1/2 times of those of Simulation 2. The inset in Fig. 5(a) shows the profile of the excited source in the time domain, i.e. the five-cycle sinusoidal acoustic pulses with the central frequency f = 189 kHz, which is in accordance with the experimental source.

We show the calculated $|u_z|$ in the time domain in Fig. 5(a). Note that in Fig. 5(a), we show the raw signals retrieved from P2. The results show four poles at $\theta = 0°$, 90°, 180°, and 270°. The experimentally measured raw signals on P2 are shown in Fig. 5(b). This map has four parts separated by three dips along 45°, 135°, and 225°, giving rise to four poles in a way similar to the numerical results in Fig. 5(a). The rough surface of the top of the steel pillar P2, as compared to the aluminum plate where the source signals are measured, account for the smaller experimental amplitude. Besides, one must consider the experimental imperfection when locating the measured points as a consequence of the rough surface condition. Nevertheless, the experimental polar diagram and map in time domain of $|u_z|$ gives the direct proof of the existence of quadrupolar WGMs in hollow pillars.

In the next, we turn to the Z-shaped waveguide for which the route line of hollow pillars features two 90° corners. Figure 6(a)
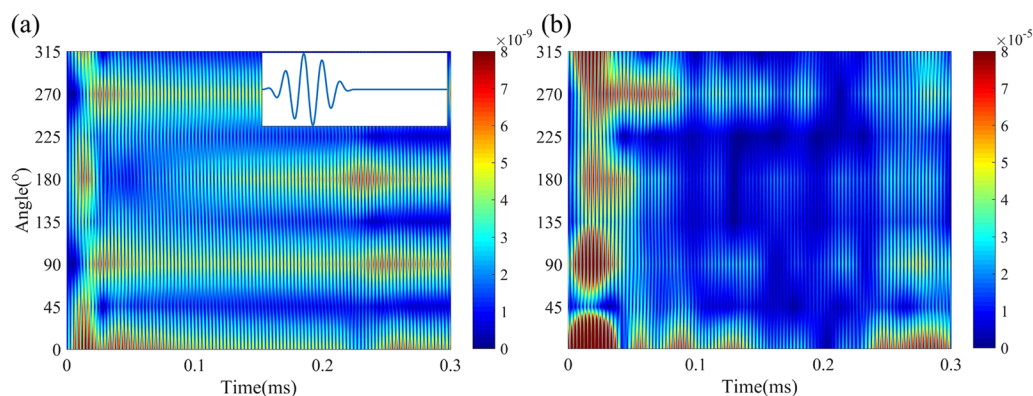
FIG. 5. (a) Map of calculated $|u_z|$ on P2 in time domain. (b) Map of measured $|u_z|$ on P2.
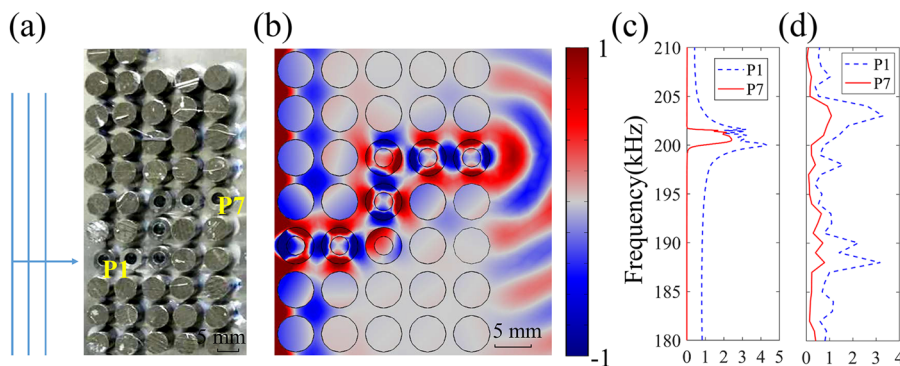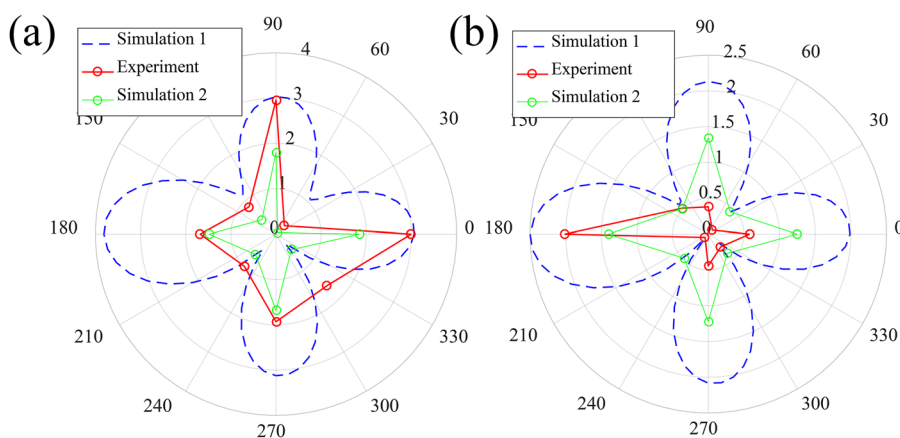
FIG. 6. (a) Top view of Z-shaped waveguide with the d_2 = 2.56 mm. (b) Numerical distribution of normalized u_z at f = 201 kHz. (c) Calculated and (d) measured average $|u_z|$ on top of P1 and P7.

shows the top view of the experimental sample whose geometric parameters are the same as the straight waveguide except for the inner diameter of hollow pillars d_2 = 2.56 mm. The incident A_0 wave impinges the sample from left side. The inlet and outlet hollow pillars are labeled as P1 and P7, respectively. We then performed the numerical simulation by FEM. Figure 6(b) shows the computed distribution of normalized u_z versus the amplitude of incident wave when f = 201 kHz, wherein the wave energy is guided forward in the designed route line through the quadrupolar oscillation of the hollow pillars. We also measured the u_z on top of hollow pillars by using the PP piezoelectret film and the laser ultrasonic technique. Figures 6(c) and 6(d) show the calculated and measured average $|u_z|$ on top of P1 (blue dashed line) and P7 (red solid line), respectively, derived from the eight points the same as before. From these two figures, the calculated maximum $|u_z|$ of both P1 and P7 appears around 201 kHz, corresponding well to WGMs, and the measured peak appears around 203 kHz in good agreement with the numerical results.

Figure 7(a) shows the experimental polar diagram of $|u_z|$ at f = 203 kHz by the red solid line. One can see that the red line has approximately four convex poles located at θ = 0°, 90°, 180°, and 270° as before, which agrees with the numerical counterpart calculated in frequency domain as shown by the blue dashed line when f = 201 kHz. However, the node at 315° is almost of equal amplitude to the peak at 180°. The polar diagram of $|u_z|$ at 201 kHz calculated

in time domain is shown as green solid line in Fig. 7(a). The result shows that the amplitudes of Simulation 2 are much smaller than Simulation 1, except that the peaks 180° and 270° has almost the same amplitude of experiment. It is noteworthy that the experimental result has the similar characteristic as the Simulation 2: large amplitude at nodes 135°, 225° and 315°, small amplitude at node 45°.

Furthermore, Fig. 7(b) shows the numerical (blue dashed line, frequency domain; green solid line, time domain) and experimental (red solid line) polar diagrams of $|u_z|$ at the eight points on top of P7, respectively. The calculated $|u_z|$ at f = 200 kHz in both the frequency domain and time domain feature four spots near θ = 0°, 90°, 180°, and 270°, indicating the occurrence of quadrupolar WGMs, whereas the experimental polar diagram of $|u_z|$ features no more clear quadrupolar pattern on P7. Despite the unavoidable sample imperfection, this discrepancy can be understood from the following points of view. When comparing the experimental results with Simulation 2, the experimental peak at 0° is half the amplitude as Simulation 2, being similar to the case for the straight waveguide in Fig. 4. The peak at 270° can also be recognized as one pole for its larger amplitude in comparison to the two adjacent nodes at 225° and 315°. The largest peak amplitude at 180° is due to the resonance and enhancement of two adjacent pillars, the same reason for the appearance of peak at 0° in Fig. 7(a). So that the experimental polar diagram in Fig. 7(b) shows at least three poles. Despite the

FIG. 7. Polar diagram of computed $|u_z|$ at 201 kHz in frequency domain (blue dashed line), in time domain (green solid line) and measured $|u_z|$ at 203 kHz (red solid line) on top of (a) P1 and (b) P7.
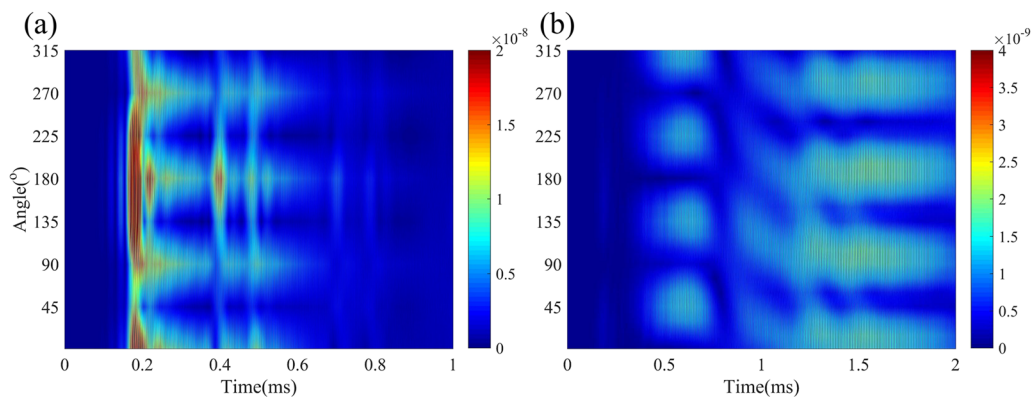
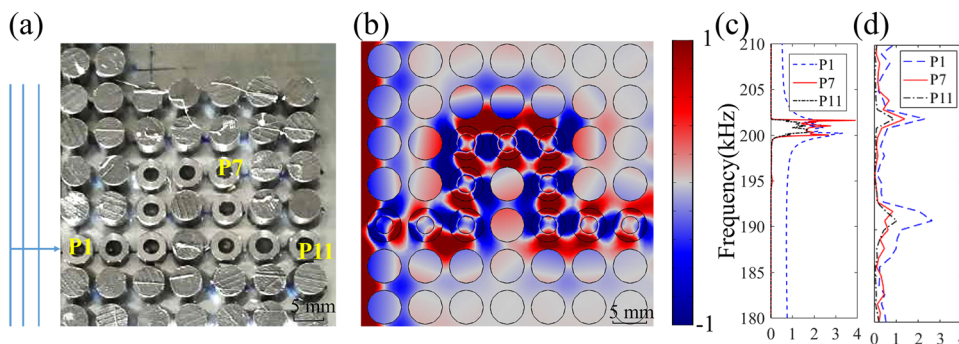**FIG. 8**. Map of calculated $|u_z|$ on (a) P1 and (b) P7 in time domain.

FIG. 9. (a) Top view of π-shaped waveguide whereby the d_2 = 2.56 mm, and (b) computed distribution of normalized u_z when f = 200 kHz. (c) Calculated and (d) measured average $|u_z|$ on top of P1 (blue dashed line), P7 (red solid line) and P11 (black dot-dashed line), respectively.

unavoidable imperfection in experimentation, the experimental proof of the existence of quadrupolar in P7 is given above, taking no account of small peak at 90° in Fig. 7(b).

We show the calculated map of $|u_z|$ in time domain in Fig. 8(a) for P1 and in Fig. 8(b) for P7. Figure 8(a) shows clearly four poles at θ = 0°, 90°, 180°, and 270°. Figure 8(b) shows that the first four maximum amplitudes appear at 45°, 135°, 225° and 315° when P7 vibrates, and that another four poles appear at 0°, 90°, 180°, and 270°. This map illustrates that P7 resonates after a long time and the position of maximum amplitudes have a shift. During the experiment, the signals received by LDV don't contain so long time as Simulation 2. Therefore, one can see the discrepancies between experimental and numerical results for P7, besides the unavoidable sample imperfections in experiment.

After that, we built the π-shaped waveguide whereby the route line of hollow pillars features three 90° corners as shown in Fig. 9(a). The pillars have the same geometrical parameters as those in the Z-shaped waveguide. Figure 9(b) shows the distribution of normalized u_z at a selected frequency f = 200 kHz whereby the hollow pillars exhibit quadrupolar WGMs. We repeat the experimental characterization by using the PP piezoelectret film and LDV, and measured the u_z on top of hollow pillars. Figures 9(c) and 9(d) show the calculated and measured average amplitude of $|u_z|$ on top of P1 (blue dashed line), P7 (red solid line) and P11 (black dot-dashed line), respectively. In Fig. 9(c), the maxima of $|u_z|$ on top of P1, P7 and P11 appear around 200 kHz that corresponds well to frequency position

of WGMs in Fig. 1(a), while in Fig. 9(d) the measured counterparts of $|u_z|$ occur around 203 kHz, in good agreement with the experimental result. In Fig. 9(d), one can also see a relatively high value for $|u_z|$ at around 192 kHz on top of P1, P7, and P11, which is unexpected from the numerical results in Fig. 9(c). We attribute this phenomenon to the broad frequency range of the wave source and the imperfection of samples, which allows possible mode conversion or interference between forward and scattered waves inside the waveguide, with the occurrence of 90° corners. However, the waves are guided forward from P1 to P11 through the WGMs although the amplitude decreases a little bit from P1 to P11 due to the reflections inside the waveguide.

V. CONCLUSIONS

In summary, we built three different waveguides by adding hollow pillars along the gradually complicated route paths, i.e. the straight waveguide, Z-shaped waveguide and π-shaped waveguide. We experimentally investigated the performance of hollow pillars in these waveguides by measuring the displacement on top of pillar through the combination of air-coupled method, laser ultrasonic technique, and another approach based on PP piezoelectret film. The quadrupolar pattern was experimentally observed for the displacement on top of hollow pillars in both the straight and Z-shaped waveguides, in good agreement with the numerical results. In addition, the efficiency of waveguides with gradually more 90° corners is

confirmed and is helpful for designing complex waveguides whose route line is in any path. This work revealed the actual performance of hollow pillars in PCs based waveguides in an experimental way, which is helpful for fine regulation of vibration in resonators and the optimization of acoustic circuits.

ACKNOWLEDGMENTS

REFERENCES

[1] M. Maldovan, Nature **503**(7475), 209 (2013).

[2] L. Y. Zheng, Y. Wu, X. Ni, Z. G. Chen, M. H. Lu, and Y. F. Chen, Appl. Phys. Lett. **104**, 161904 (2014).

[3] H. F. Zhu and F. Semperlotti, Phys. Rev. Appl. **8**, 064031 (2017).

[4] M. Addouche, M. A. Al-Lethawe, A. Choujaa, and A. Khelif, Appl. Phys. Lett. **105**, 023501 (2014).

[5] I. A. Veres, T. Berer, O. Matsuda, and P. Burgholzer, J. Appl. Phys. **112**, 053504 (2012).

[6] S. Villa-Arango, D. B. Sanchez, R. Torres, P. Kyriacou, and R. Lucklum, Sensors-Basel **17**(9), 1960 (2017).

[7] L. Zigoneanu, B. I. Popa, and S. A. Cummer, Phys. Rev. B **84**, 024305 (2011).

[8] A. Khelif, A. Choujaa, S. Benchabane, B. Djafari-Rouhani, and V. Laude, Appl. Phys. Lett. **84**(22), 4400 (2004).

[9] S. Benchabane, O. Gaiffe, R. Salut, G. Ulliac, V. Laude, and K. Kokkonen, Appl. Phys. Lett. **106**, 081903 (2015).

[10] M. G. Baboly, A. Raza, J. Brady, C. M. Reinke, Z. C. Leseman, and I. El-Kady, Appl. Phys. Lett. **109**, 183504 (2016).

[11] M. R. Foreman, J. D. Swaim, and F. Vollmer, Adv. Opt. Photonics **7**(2), 168 (2015).

[12] H. J. Chen, J. H. Guo, and K. D. Zhu, IEEE Sens. J. **15**(6), 3375 (2015).

[13] S. H. Huang, S. Sheth, E. Jain, X. F. Jiang, S. P. Zustiak, and L. Yang, Opt. Express **26**(1), 51 (2018).

[14] A. Khelif, P. A. Deymier, B. Djafari-Rouhani, J. O. Vasseur, and L. Dobrzynski, J. Appl. Phys. **94**(3), 1308 (2003).

[15] Y. Pennec, B. Djafari-Rouhani, J. O. Vasseur, A. Khelif, and P. A. Deymier, Phys. Rev. E **69**, 046608 (2004).

[16] Y. B. Jin, N. Fernez, Y. Pennec, B. Bonello, R. P. Moiseyenko, S. Hemon, Y. D. Pan, and B. Djafari-Rouhani, Phys. Rev. B **93**, 054109 (2016).

[17] W. T. Yuan, J. F. Zhao, B. Bonello, B. Djafari-Rouhani, X. Q. Zhang, Y. D. Pan, and Z. Zhong, Phys. Rev. Appl. **10**, 034010 (2018).

[18] J. F. Zhao, W. T. Yuan, B. Bonello, B. Djafari-Rouhani, Y. D. Pan, and Z. Zhong, Sci. China Technol. Sc. **62**(3), 458 (2019).

[19] Z. Wang, S. Y. Yu, F. K. Liu, H. Zhang, M. H. Lu, and Y. F. Chen, J. Phys. D Appl. Phys. **51**, 255104 (2018).

[20] S. Benchabane, R. Salut, O. Gaiffe, V. Soumann, M. Addouche, V. Laude, and A. Khelif, Phys. Rev. Appl. **8**, 034016 (2017).

[21] D. B. Zhang, J. F. Zhao, B. Bonello, F. L. Zhang, W. T. Yuan, Y. D. Pan, and Z. Zhong, J. Phys. D Appl. Phys. **50**, 435602 (2017).

[22] D. B. Zhang, J. F. Zhao, B. Bonello, L. B. Li, J. X. Wei, Y. D. Pan, and Z. Zhong, AIP Adv. **6**, 085021 (2016).

[23] Y. Xue and X. Q. Zhang, IEEE T. Dielect. El. In. **25**(3), 808 (2018).

[24] Y. Xue, X. Q. Zhang, J. Zheng, T. Liu, and B. Zhu, IEEE T. Dielect. El. In. **25**(1), 228 (2018).